Nuclear Science and Techniques (2024) 35:181
https://doi.org/10.1007/s41365-024-01560-9

Study on the thermo-hydraulic behaviors of the new-pattern fuel assembly in lead-based fast reactors based on OpenFOAM

Yun-Xiang Li[1] · Run-Sheng Yang[1] · Yue Li[1] · Xing-Kang Su[2] · Zi-Nan Huang[1] · Lu Meng[1] · Song Li[1] · Bin Xi[1] · You-Peng Zhang[1] · Lu Zhang[3] · Wei Jiang[3]

Received: 6 January 2024 / Revised: 23 March 2024 / Accepted: 27 March 2024 / Published online: 27 September 2024

Abstract

To improve the heat transfer efficiency of the coolant in lead-based fast reactors, this study optimized the configuration and rotational direction of the spacer wires in fuel assemblies to design a new-pattern fuel assembly. This study conducted detailed comparisons between traditional and new pattern fuel assembly rod bundles utilizing the open-source computational fluid dynamics platform, OpenFOAM. The results indicated that the new design may significantly reduce the pressure drop along the rod bundle, which is beneficial for lowering the pressure drop. Furthermore, this new design improved coolant mixing in the subchannels, which facilitated a more uniform temperature distribution and lower thermal gradients at the assembly outlet. These factors collectively reduced the thermal fatigue and creep in nearby internal components. Overall, the new-pattern fuel assembly proposed in this study may have better heat transfer performance, thereby enhancing the Integrated Thermal-Hydraulic Factor by 48.2% compared to the traditional pattern.

Keywords Spacer wires · Enhanced coolant mixing · OpenFOAM · CFD simulations

1 Introduction

Nuclear energy is widely considered a clean and efficient energy source that plays a pivotal role in reducing global carbon emissions through power generation and supporting sustainable human development. In 2002, the American Nuclear Society identified six advanced fourth-generation nuclear reactor designs [1], highlighting significant simplifications in the structure of lead-based fast reactors [2]. Lead-based fast reactors are notable for their efficient nuclear fuel transmutation, economic viability, and inherent safety [3]. However, severe accidents with core meltdowns may result in high-reactivity excursions that must be mitigated [4–9]. Consequently, substantial research and development efforts have been invested globally, with notable projects such as the China Initiative Accelerator-Driven System (CiADS), launched in 2015 [10]. The CiADS, comprising an accelerator, a spallation target, and a subcritical reactor [11–14], utilizes a liquid lead–bismuth alloy as a cooling medium in its subcritical fast neutron reactor. A common feature of most lead-based fast reactors is the use of wire-wrapped technologies for fuel-rod positioning. This technology facilitates coolant flow and heat transfer, which may create continuous axial swirls around fuel rods [15], thereby enhancing mixing and heat transfer across subchannels. Considering these complexities, the thermal-hydraulic design within the reactor core must be explored for the safe operation of fuel assemblies and other components. This necessitates detailed research on the flow characteristics of wire-wrapped fuel assemblies.

This work was supported partly by the Ministry of Science and Technology of the People's Republic of China (No. 2020YFB1902100), the China Postdoctoral Science Foundation (No. 2023M731458), the Science and Technology Program of Gansu Province, China (No. 23JRRA1099), and the Postdoctoral Fellowship Program of CPSF (No. GZB20230278). This research was financially supported by the Shanghai Municipal Commission of Economy and Informatization (No. GYQJ-2018-2-02).

✉ You-Peng Zhang
zhangyp@fudan.edu.cn

[1] Institute of Modern Physics, Fudan University, Shanghai 200433, China

[2] School of Nuclear Science and Technology, Lanzhou University, Lanzhou 730000, China

[3] Institute of Modern Physics, Chinese Academy of Sciences, Lanzhou 730000, China

International researchers have extensively employed experimental methods to investigate pressure drop and turbulent mixing in wire-wrapped fuel assemblies. Arwikar et al. conducted experiments on a 61-pin wire-wrapped fuel assembly using water as the working fluid. They reported that spacer wires can significantly exacerbate the pressure drop [16]. Similarly, Masahiro et al. leveraged particle image velocimetry (PIV) technology to analyze the velocity distribution within the subchannels of a wire-wrapped fuel assembly and detected the vortex flow near the spacer wires on the transverse velocity contours [17]. Kim et al. explored the single-phase flow velocity distribution in a 37-pin fuel assembly and observed a shift in the maximum coolant velocity toward the corner channels along the pin bundle [18]. Pacio et al. performed heat transfer experiments on a 19-pin wire-wrapped fuel assembly at the KALLA laboratory, thereby contributing to the validation of computational fluid dynamics (CFD) calculations [19]. Wang et al. investigated the flow field in a single-pin wire-wrapped bundle within a square assembly and discovered vortex flow patterns in the wire-wrapped region. Their research indicated a decrease in the maximum transverse velocity and an increase in the maximum crossflow velocity with decreasing axial height [20].

The shielding effect of lead-bismuth radiation poses challenges when X-ray devices are used for internal flow field studies in components [21]. Consequently, researchers have developed numerical methods for analyzing fuel assemblies. Su et al. developed computational equations for lead–bismuth material properties, incorporating deduced principles and thermal properties such as melting and boiling points, density, specific heat capacity, viscosity, and thermal conductivity, supplemented by experimental data from other researchers [22]. Wu et al. examined the impact of factors such as coolant type, support structure, and aspect ratio on coolant sloshing within reactor vessels using a bidirectional fluid–structure interaction finite element method. They found negligible effects of fluid dynamic viscosity on large-scale reactor fluid–structure interactions [23]. Gu et al. introduced MPC-lead–bismuth eutectic (LBE), a multiphysics field coupling software for the thermal hydraulic analysis of reactors with liquid LBE cooling in a pool configuration [24]. Liu et al. applied five turbulent Prandtl number models to predict heat transfer in the subchannels of rod bundles containing low Prandtl number fluids [25]. Roozbeh et al. developed a semi-analytical method corroborated by a steady-state CFD analysis. They demonstrated marked improvements over traditional approaches [26]. Ahmad et al. utilized the RANS model to study three configurations: a 7-rod bundle, a 7-rod bundle with wire wrapping, and a 19-rod bundle with wire wrapping. They noted the influence of the wire wrap on the local Nusselt number in the subchannels [27]. Gajapathy et al. conducted simulations on various fuel assemblies with wire wrapping and observed that larger wire diameters and smaller pitches increased the friction factors and Nusselt numbers [28]. Hamman et al. identified a 10–15% discrepancy in pressure drop calculations compared with empirical formulas influenced by turbulence and geometric modeling [29]. Fricano et al. modeled a 19-rod bundle in a sodium-cooled fast reactor. They achieved close agreement with the experimental data within the rod bundle, but not at the outlet [30]. Jeong et al. applied the SST turbulence model to a 37-rod bundle assembly and aligned the simulated results with the friction factor Reynolds number correlation [31]. Dovizio et al. confirmed the applicability of the RANS method to wire-wrapped assembly models, which was corroborated by PIV experimental data [32]. Shaopeng et al. developed a CFD solver based on the k–ϵ-$k\theta$-$\epsilon\theta$ model, designed to simulate the flow and thermal dynamics of liquid lead–bismuth. The research revealed that the rotational influence of the wire wraps significantly enhanced the lateral flow and mixing in the rod bundle. Such interactions yielded an asymmetric distribution in both the velocity and temperature fields, highlighting the intricate dynamics involved [33]. Hanrui et al. explored the complexities of the flow and heat transfer between claddings in liquid-metal-cooled reactors. They revealed a detailed interplay between the heat transfer characteristics and flow dynamics, which were significantly affected by the interaction of the intra-wrap flow and wire-wrap mixing. This study uncovered nuanced aspects of the thermal and fluid behavior in these environments [34]. Octavio et al. utilized the RANS model to simulate flow phenomena in wire-wrapped rod bundles under transitional and turbulent conditions, predicting axial pressure drops across various Reynolds numbers [35]. Octavio et al. utilized the URANS approach to estimate the axial friction coefficient in wire-wrapped fuel assemblies. The results suggested that the k–ω SST model was effective for computational simulations during the transitional phase [36]. Octavio et al. employed the RANS k–ϵ realizable model for high-precision thermal-hydraulic performance evaluations of wire-wrapped fuel assemblies with complex geometries [37]. Yaodi et al. analyzed the effects of various wire-wrap configurations on the thermal-hydraulic properties of sodium-cooled fast reactor fuel assemblies by conducting CFD simulations [38]. Xiao et al. introduced an equivalent method for fuel assembly analysis and conducted a numerical investigation into the impact of low-flow convective heat transfer in oscillatory conditions. They employed the k–ω SST turbulence model coupled with an additional force model [39]. Li et al. used the k–ω SST turbulence model to assess flow and heat transfer in CiADS reactor fuel assemblies. They observed that wire wrapping increased the pressure drop along the rod bundle and enhanced coolant flow heat transfer [40].

In conclusion, although extensive numerical research has been conducted on parameters such as the pitch-to-diameter

ratio (P/D) and number of fuel rods in assemblies, studies focusing on the spacer wire direction and arrangement within these assemblies are scarce. Considering the intricate nature of spacer wire structures and the challenges in developing two-phase flow models, OpenFOAM, an open-source software package, was employed to optimize the spacer wire configurations in the CiADS fuel assembly. Concurrently, numerical analyses were performed to evaluate factors including pressure drop, temperature, transverse secondary flow, convective heat transfer coefficient, and overall thermal-hydraulic characteristics of the newly designed fuel assembly model.

2 Models and methodologies

2.1 Governing equations

CFD operates fundamentally by converting fluid flow challenges into a set of discrete equations derived using numerical methods. These equations are generally based on the Navier–Stokes equations and encapsulate the principles of continuity, momentum conservation, and other core fluid physics laws. OpenFOAM, C++-based open-source CFD software, offers distinct advantages over conventional commercial CFD tools. Its open-source framework enables users to create custom solvers tailored to specific requirements, thereby enhancing the customization flexibility. The solver developed for this research utilized OpenFOAM V7 and was compiled within the Ubuntu 18.04 system environment. The governing equations for mass, momentum, and energy conservation in the context of the liquid lead–bismuth flow and heat transfer are as follows:

$$\frac{\partial u_j}{\partial x_j} = 0, \tag{1}$$

$$\frac{\partial u_i}{\partial t} + u_j\frac{\partial u_i}{\partial x_j} = -\frac{1}{\rho}\frac{\partial p}{\partial x_i} + \frac{\partial}{\partial x_j}\left(\nu\frac{\partial u_i}{\partial x_j}\right) - \frac{\partial}{\partial x_j}\overline{u_i'u_j'} + f_i, \tag{2}$$

$$\frac{\partial T}{\partial t} + u_j\frac{\partial T}{\partial x_j} = \frac{\partial}{\partial x_j}\left(\alpha\frac{\partial T}{\partial x_j}\right) - \frac{\partial}{\partial x_j}, \tag{3}$$

where u_i, p, and T denote the Reynolds-averaged velocity, pressure, and temperature, respectively, ρ, ν, and α represent the fluid's density, molecular kinematic viscosity, and molecular thermal diffusivity, respectively. $\overline{u_i'u_j'}$ and $\overline{u_j'T'}$ represent the unknown terms of Reynolds stress and Reynolds heat flux that are closed by additional models, respectively, and f_i signifies the gravity source term.

During the calculation, an isotropic eddy viscosity model was employed to approximate the Reynolds stress term $\overline{u_i'u_j'}$:

$$\overline{u_i'u_j'} = -\nu_t\left(\frac{\partial u_i}{\partial x_j} + \frac{\partial u_i}{\partial x_j}\right) + \frac{2k}{3}\delta_{ij}, \tag{4}$$

where ν_t is the turbulent eddy viscosity and k is the turbulent kinetic energy. The simple gradient diffusion hypothesis [41] (SGDH) was used to simulate the Reynolds heat flux term $\overline{u_j'T'}$:

$$\overline{u_j'T'} = -\alpha_t\frac{\partial T}{\partial x_j}, \tag{5}$$

where α_t is the turbulent thermal diffusivity. In the Reynolds analogy assumption, the ratio of turbulent eddy viscosity ν_t to turbulent thermal diffusivity α_t is known as the turbulent Prandtl number Pr_t. The low Prandtl number characteristic of liquid lead–bismuth results in a notably thicker thermal boundary layer compared to its velocity boundary layer. This markedly alters its heat transfer properties relative to conventional fluids. For liquid lead-bismuth, the turbulent Prandtl number [42, 43] typically exceeds 0.85. In this analysis, the impact of turbulence was considered, which necessitated an adjustment to the liquid lead-bismuth Prandtl number [44].

$$\begin{aligned} Pr_t &= \begin{cases} 4.12, & P_e \le 1000 \\ \frac{0.01P_e}{\left[0.018P_e^{0.8}-(7-A)\right]^{1.25}}, & 1000 \le P_e \le 6000 \end{cases} \\ A &= \begin{cases} 4.5, & P_e \le 1000 \\ 5.4 - 9\times10^{-4}P_e, & 1000 \le P_e \le 2000 \\ 3.6, & P_e \ge 2000 \end{cases} \end{aligned} \tag{6}$$

Figure 1 illustrates the CFD calculation methodology. OpenFOAM, an open-source computational fluid dynamics software, offers a wide array of operators for solving partial differential equations. In this study, the control equations for various physical quantities were defined on the OpenFOAM platform, facilitating their utilization in numerical calculations. The field variable declaration file createFields.H was expanded to include the necessary volume scalar fields. These control equations were integrated using OpenFOAM's operators. The software supports both explicit and implicit computational methods in its conservation equations. It employs a second-order discretization approach to ensure accuracy in quantifying the physical properties. Specifically, a temperature volume scalar was incorporated into the temperature conservation equation for liquid lead–bismuth, and a dedicated subprogram, TEqn.H, was developed to solve this equation. In addition, the pressure Poisson equation was addressed using a subprogram, pEqn.H, based on the

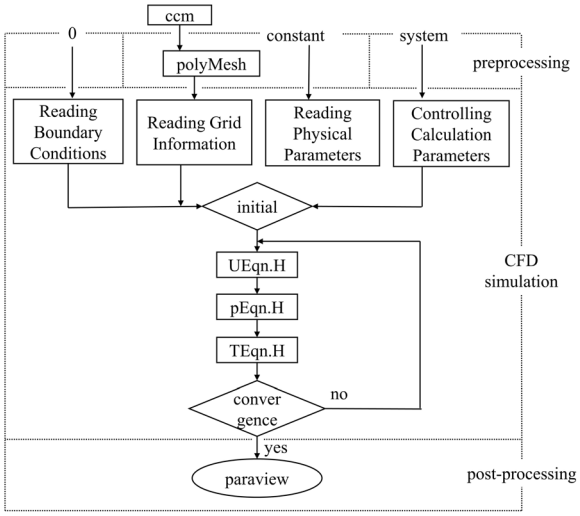

Fig. 1 Flowchart for the calculation of heat transfer in liquid lead–bismuth single-phase flow based on OpenFOAM

SIMPLE algorithm. Following the described process, calculations for heat transfer in a single-phase liquid lead–bismuth single-phase flow can be conducted.

2.2 Geometric model and mesh division

In lead-based fast reactors, the fuel rods are typically configured in a triangular layout to create hexagonal assemblies. These assembly subchannels can be categorized into three types: internal, edge, and corner. In this study, the fuel assembly parameters of the CiADS [45, 46] subcritical reactor were used for the simulations. By maintaining the diameters of the fuel rods and spacer wires, the structure of the single-box fuel assembly, which originally comprised 61 rod bundles, was scaled down to 19 rod bundles, with the assembly box side length reduced to 40.4 mm. The regular hexagonal fuel assembly comprised 18 fuel rods and a central stainless-steel rod, which functioned as a locking mechanism to prevent the displacement of the assembly in the liquid lead/lead–bismuth alloy. The simulation focused on the active region of the fuel assembly extending to an axial height of 360 mm.

The fuel rods in lead-based fast reactors are typically aligned using wire-wrap structures. In traditional designs, each rod is encased in a single spacer wire, and all rods are wound clockwise. This study introduced an innovative fuel assembly pattern that revised the wire-wrap winding technique and layout to improve coolant mixing and reduce pressure drop. Figure 2 illustrates a comparison of the active regions in both the traditional and new pattern fuel assemblies. In the novel design, the central stainless-steel rod remained unwrapped, whereas the six adjacent fuel rods featured wire wraps wound counterclockwise. This

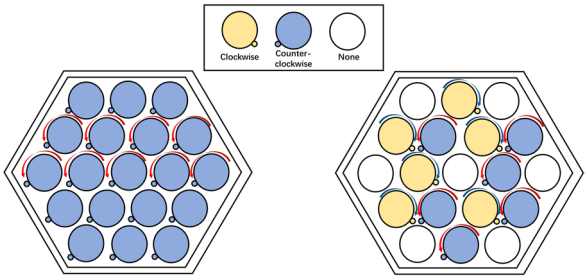

Fig. 2 (Color online) Spacer wire distribution in the traditional and new-pattern fuel assemblies

Table 1 Geometry parameters of the traditional and new-pattern fuel assemblies

Parameter name	Traditional pattern	New pattern
Number of fuel rods, N_r	18	18
Number of spacer wires, N_W	19	12
Rod length, L_{heat} (mm)	360	360
Length of assembly box side, L_A (mm)	40.4	40.4
Rod diameter, D (mm)	13.1	13.1
Pin pitch, P (mm)	15.1	15.1
Helical pitch, H (mm)	144	144
Helical wire diameter, D_w (mm)	2	2

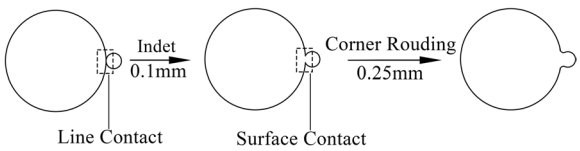

Fig. 3 Simplified wired pin model

alternating winding pattern was aimed at augmenting lateral mixing between subchannels without requiring additional vortex generators. In addition, the fuel rods at the periphery of the new pattern assembly were unwrapped, which is a strategy anticipated to lower the pressure drop along the assembly. Table 1 lists the geometric details of the active regions for both the traditional and new pattern assemblies.

This study introduced a simplified approach to mitigate the issue of line contact between the spacer wires and fuel rods, which often results in sharp corners at the contact points, as depicted in Fig. 3. By maintaining the original diameters of both the fuel rods and spacer wires, the spacer wire was recessed by 0.1 mm toward the center of the rod [35, 47]. Furthermore, to enhance the quality of the resulting mesh, a 0.25-mm fillet was implemented at the wire wrap and fuel–rod contact points.

Table 2 Method of grid encryption

	Number of boundary layer and grid layers	Total thickness of prismatic layer (mm)	Grid growth rate	Expected y+
The area near the wall	4 layers	0.03	1.2	< 1
The area near the assembly box	4 layers	0.09	1.2	< 1

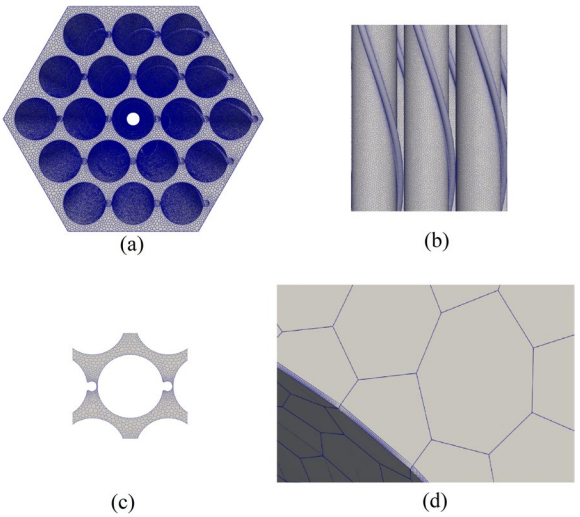

Fig. 4 (Color online) Grid division

Generating structured meshes for the complex geometry of a wire-wrap surface characterized by large curvatures is challenging. Consequently, this simulation employed polyhedral meshes for the fuel assembly model. The mesh was refined near the wall and the assembly box, as presented in Table 2. Mesh quality was assessed using OpenFOAM's "checkMesh" method, confirming that the mesh satisfied computational requirements. Figure 4 illustrates the mesh division, and Fig. 4a shows the cross-sectional mesh distribution of the fuel assembly. Figure 4b presents the mesh distribution along the axial direction. Figure 4c focuses on a wire-wrap structure with a localized zoomed-in view. Figure 4d illustrates the boundary-layer mesh.

2.3 Boundary conditions setting and grid independence analysis

Effective numerical simulations necessitate the assignment of appropriate boundary conditions to each boundary, tailored to reflect actual operating conditions. In this study, the boundary conditions were established in accordance with the methodologies outlined in the CiADS [45, 46] project, as detailed in Table 3.

Table 3 Boundary conditions for the fuel assembly

Boundary	Boundary conditions
Inlet	Average temperature of the inlet was 553.1 K
	The mass flow rate of the inlet was 17.07 kg/s
Outlet	Pressure outlet with a gauge pressure of 0 Pa [48]
fuel rods	The linear power density was set as Fig. 5
One stainless steel rod	Adiabatic and no-slip surface
Spacer wires	Adiabatic and no-slip surface [49]
Assembly box	Adiabatic and no-slip surface

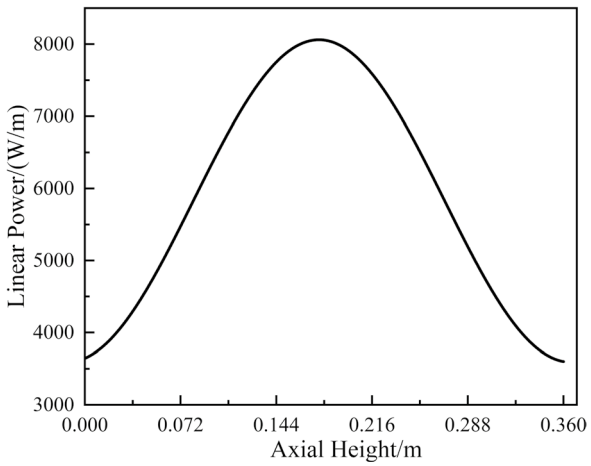

Fig. 5 Axial linear power distribution of all fuel rods

Table 4 Grids for independence studies

	The number of grids	Min y+	Max y+	Average y+	Time (s)
Case1	6,586,478	0.07515	1.662	0.4293	21,451
Case2	8,457,138	0.04909	1.797	0.4621	34,687
Case3	13,039,537	0.04666	1.941	0.5002	56,843

Three grid sets of varying densities were created for the traditional 19-rod bundle fuel assembly model with spacer wires. A grid-independence analysis assessing the axial temperature variation on the cladding surface of fuel rod 4 was performed to compare the grids. Table 4 lists the grid counts, $y+$ values, and computation times for each grid set, with all sets achieving an average $y+$ value of less than 1. Figure 6 shows a comparison of the peak temperatures on fuel rod 4's cladding surface, revealing consistent temperature development trends and closely matching temperature

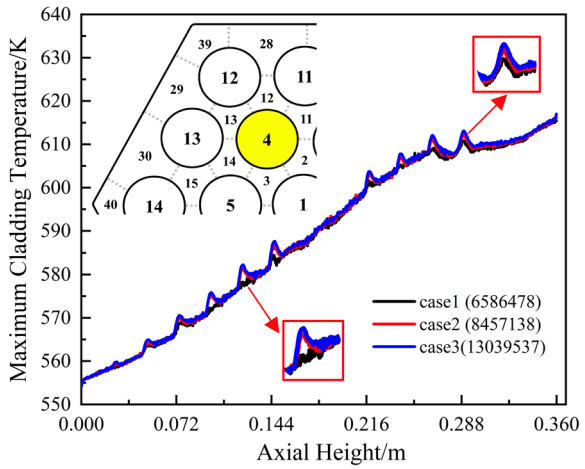

Fig. 6 (Color online) Comparison of the maximum surface temperature of fuel rod 4 calculated using three sets of grids

values across all grid sets under identical computational conditions. Scheme 2 was selected for further calculations because of the balance between computational accuracy and efficiency.

2.4 Coolant thermal physical parameters and turbulence model

In this analysis, liquid lead–bismuth alloy was used as the coolant. The distinct thermal properties of lead–bismuth facilitate behaviors that differ from those of traditional coolants. Considering the ability of liquid lead and liquid bismuth to mix in any proportion, the physical properties of the most commonly used alloy, comprising 44.5% Pb and 55.5% Bi, were expressed using a polynomial equation. Following the guidelines of the OECD/NEA [50], specific expressions for the thermal property parameters of lead–bismuth have were selected as follows:

Density (kg/m^3) is given as

$$\rho_{\mathrm{LBE}} = 11096 - 1.3236T; \tag{7}$$

Constant-pressure specific heat capacity $(J/(kg \cdot K))$ is given as

$$C_{\mathrm{p,LBE}} = 159.0 - 0.0272T + 7.12 \times 10^{-6}T^2; \tag{8}$$

Dynamic viscosity (Pa s) is given as

$$\mu_{\mathrm{LBE}} = 0.00456 - 7.03 \times 10^{-6}T + 3.61 \times 10^{-9}T^2; \tag{9}$$

Thermal conductivity, $(W/(\mathrm{m\,K}))$ is given as

$$\lambda_{\mathrm{LBE}} = 3.61 + 1.517 \times 10^{-2}T - 1.741 \times 10^{-6}T^2. \tag{10}$$

The empirical relationships between these physical parameters are applicable under normal atmospheric pressure. The uncertainty in the physical properties of the lead–bismuth eutectic alloy is attributed to the variability of its physical and chemical properties under different conditions and inherent measurement uncertainty. Considering the alloy compositions of 44.5% Pb and 55.5% Bi, it was assumed that the composition ratio remained constant during the flow and heat transfer processes, rendering the physical properties of the alloy highly temperature-dependent. This research demonstrated that temperature variations significantly affected the physical properties of the lead–bismuth alloys, thereby impacting the dynamics of flow and heat transfer. In addition, the accuracy and reliability of different measurement techniques and devices further contributed to data uncertainty. However, through simulation calculations, it was possible to obtain precise data measurements at each grid point, effectively reducing uncertainty.

Each turbulence model was tailored to specific conditions. The k–ε model effectively simulates fully developed turbulent flows, whereas the k–ω model excels in accurately depicting free shear, attached boundary layer, and moderate separation turbulence. The k–ω SST model [51], introduced by Menter, combines the strengths of both: employing the k–ω model in the near-wall region to capture shear flows and the k–ε model in regions further from the wall, thereby accurately representing fully developed turbulence. A comparison with the large eddy simulation (LES) results of Merzari et al. indicated superior alignment of the k–ω SST model with actual conditions compared to the k–ε model [52]. Consequently, the k–ω SST turbulence model was selected for this analysis. It is defined by the following five equations.

$$\frac{\partial(\rho\omega)}{\partial t} = \frac{\partial}{\partial x_i}\left(\left(\mu + \sigma_k\mu_t\right)\frac{\partial k}{\partial x_i}\right) + G_\omega - \rho\beta^*\omega k \tag{11}$$

$$\begin{aligned}\frac{\partial(\rho\omega)}{\partial t} =& \frac{\partial}{\partial x_i}\left(\left(\mu + \sigma_\omega\mu_t\right)\frac{\partial k}{\partial x_i}\right) + G_k - \rho\beta\omega^2 \\ &+ 2\left(1 - F_1\right)\rho\sigma_{\omega^2}\frac{1}{\omega}\frac{\partial k}{\partial x_i}\frac{\partial \omega}{\partial x_i}\end{aligned} \tag{12}$$

$$G_k = \rho\gamma S^2 - \frac{2}{3}\rho k\frac{\partial U_i}{\partial x_i} - \frac{2}{3}\mu_{\mathrm{t}}\left(\frac{\partial U_i}{\partial x_i}\right)^2 \tag{13}$$

$$G_\omega = \rho\gamma\left(\mathrm{S}^2 - \frac{2}{3}\left(\frac{\partial U_i}{\partial x_i}\right)^2 - \frac{2}{3}\omega\frac{\partial U_i}{\partial x_i}\right) \tag{14}$$

$$F_1 = \tanh\left(\min\left(\max\left(\frac{\sqrt{k}}{0.09\omega y}, \frac{500v}{\omega y^2}\right), \frac{2k}{y^2 CD_{k\omega}}\right)^4\right) \tag{15}$$

where ρ is the density (kg/m^3), G_k is the generating term for turbulent kinetic energy k, G_ω denotes the generation term for a specific dissipation rate ω, t denotes the time term (s), x is the Cartesian coordinate system direction, μ denotes the kinetic viscosity (Pa · s), and $\mu_t = \rho kT$, where T denotes the turbulence timescale. The parameters σ_k, σ_{ω^2}, β^*, β were solved using the mixing function. Further, γ is the cross-mixing factor, S denotes the mean stress-tensor mode of the fluid, U denotes the fluid velocity (m/s), y denotes distance from the wall, v is the fluid kinematic viscosity, and $CD_{k\omega}$ is a term associated with lateral diffusion of the fluid.

2.5 Model validation

This calculation considered the effects of the coolant gravity and buoyancy. Simulations were performed with a uniformly heated coolant to ascertain the accuracy of the computational method for simulating lead-based fast reactors. The results were benchmarked against the experimental findings of Pacio [19] and the experimentally corroborated SACOS-PB subchannel program [53] aligned with the conditions of the MYRRHA reactor design. Figure 7 presents a comparison of the coolant temperatures across various subchannels at an axial height of 601.3 mm within the active zone of the fuel assembly.

Analysis of Fig. 7 revealed the temperature variations in the coolant across various subchannels on the same cross section, wherein the internal channels exhibited higher temperatures than the outer channels. Both SACOS-PB and OpenFOAM displayed close alignment in the coolant temperature across these subchannels under identical computational conditions, with a maximum relative error of less than 2%. When OpenFOAM's results were juxtaposed with the experimental data, the error margin remained under 4%. Consequently, the computational method demonstrated high precision and was suitable for calculating the single-phase flow in a new-pattern fuel assembly.

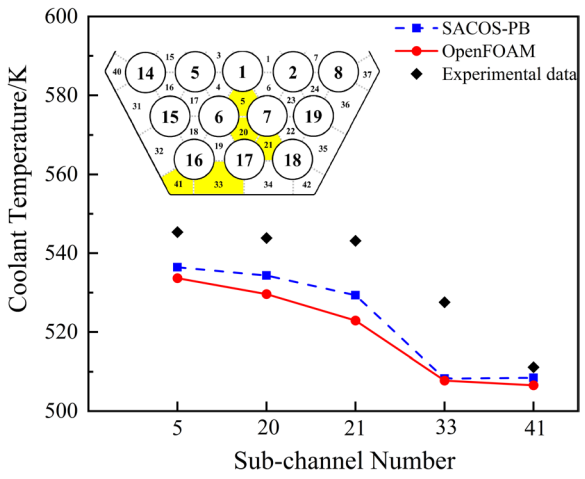

Fig. 7 (Color online) Coolant temperature distribution at the axial height of 601.3 mm in the active zone

3 Thermal-hydraulic analysis of new-pattern fuel assembly

3.1 Pressure drop analysis

The pressure drop across the fuel assembly plays a crucial role in determining the pump head and pressure-sensor range within the loop. Notably, the pressure drop in the rod bundle segment of an assembly constitutes approximately half the total pressure drop [54]. This renders its prediction a focal point for research. In this analysis, the Darcy formula was applied to validate the pressure drop in the rod bundle segment, as illustrated by the subsequent equation:

$$\Delta p = f\frac{L}{D_e}\frac{\rho v^2}{2}, \tag{16}$$

where L is the channel length, v is the coolant flow rate, and D_e is the hydraulic diameter. The friction coefficient f is a dimensionless number characterizing the fluid flow state. To assess the pressure drop in the rod bundle segment of the traditional wire-wrapped fuel assembly, three classical empirical formulas for the friction coefficient [55–57] were used. Subsequently, the pressure drop in this traditional pattern was compared with that of the novel fuel assembly model. Figure 8 illustrates the juxtaposition of the pressure drop estimations from the Darcy formula with the CFD results.

To facilitate comparison, error bars of ± 10% were incorporated into the pressure drop measurements of the rod bundle segment in the traditional fuel assembly model. In the traditional model, the initial half of the rod bundle segment aligned closely with the Novendstern empirical formula, whereas the latter half correlated well with the CTD empirical formula. At the outlet of the assembly, the deviation between the CFD results for the traditional pattern and the CTD empirical formula was 5.66%, compared to 15.20% with the Novendstern formula and 12.27% with the Remhe formula. As the coolant navigated through the spacer wires, the direction of rotation affected the area distribution, causing uneven pressure on either side of the wires. This uneven force on the fuel rod surface resulted in increased pressure at the wrap contact points, coupled with a reduced flow area and an elevated local pressure drop. Remarkably,

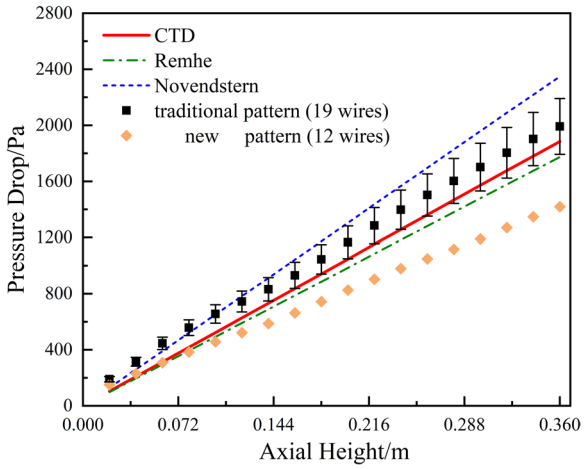

Fig. 8 Comparison of empirical formula and CFD calculation results

the maximum pressure drop reduction in the new pattern was 31.18%, with a decrease of 28.77 % at the outlet. Notably, the number of spacer wires influenced the pressure drop along the length of the assembly, and the disparity between the rod bundle segments of the traditional and new models increased with the axial height. These findings suggest that decreasing the number of spacer wires results in a lower pressure drop across the rod bundle section. In addition, the unique design of the new-pattern fuel assembly eliminated the wire wraps around the central stainless-steel rod, enhancing the axial flow area of the coolant. This arrangement diminished the flow obstruction and further reduced the pressure drop across the rod bundle section. Consequently, the new pattern design effectively reduced the pressure drop along the rod bundle segment, which is advantageous for minimizing the pump head and sensor range.

3.2 Velocity and transverse secondary flow distribution characteristics

Figure 9 illustrates the velocity distribution across the fuel assembly cross section at various axial heights for both the traditional and new models. In a traditional fuel assembly model, spacer wires create an uneven velocity distribution. The contours revealed distinct high- and low-velocity zones, with the former predominantly situated near the upstream side of the component box, in line with the rotational direction of the wrap. The coolant flow velocity in the outer channels substantially exceeded that in the inner channels, primarily owing to the variances in subchannel flow areas. The larger flow area and reduced frictional resistance adjacent to the component box contributed to the higher velocities in the outer channels. By contrast, the new model fostered a more homogeneous velocity distribution, featuring reduced maximum velocities in the outer channels compared with

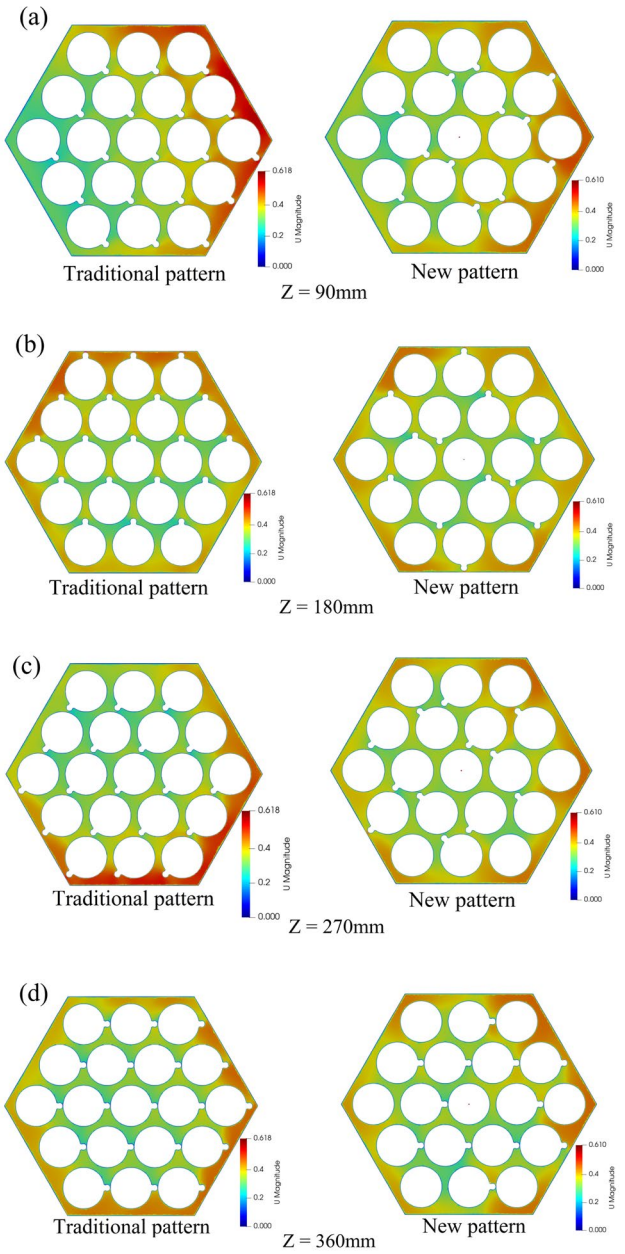

Fig. 9 (Color online) Radial velocity distribution at different axial heights. **a** $Z = 90$ mm; **b** $Z = 180$ mm; **c** $Z = 270$ mm; **d** $Z = 360$ mm

the traditional model. The variation in the wire-wrap rotation direction in the new fuel assembly pattern contributed to this effect. The absence of wire wraps on the fuel rods at the six corners of the assembly box reduced the impact on the coolant flow in the peripheral channels. Furthermore, the novel wire-wrap arrangement shifted the high-speed zone within these channels. Further, the lack of wire wraps on the central stainless-steel rod, along with the different rotation directions of the wire wraps on adjacent fuel rods, promoted vortex flow in the central subchannel. This diversity in the rotation direction increased the coolant flow velocity on

one side, thus leading to a greater pressure differential and improved coolant mixing between the subchannels.

In the fuel assembly, the inclusion of spacer wires resulted in variations in the flow area and boundaries among the subchannels, thereby creating lateral pressure gradients and prompting crossflow. The counterclockwise rotation of the spacer wires induced counterclockwise vortices within the subchannels. Using the approach devised by Wenhai [58], the transverse secondary flow intensity (TSFI) in subchannels is defined as follows:

$$\mathrm{TSFI} = \frac{1}{A}\int_A \frac{\sqrt{U_x^2 + U_y^2}}{U_z}\mathrm{d}A \tag{17}$$

where A is the sub-channel area, and U_x, U_y, and U_z represent the magnitude of the velocity components in the x, y, and z directions, respectively.

Figure 10 delineates the TSFI variations along the axial height in subchannel 1 and edge channel 25 for both the traditional and new model fuel assemblies. Distinct fluctuations characterized the TSFI distribution across different subchannels. In the traditional model, the TSFI within the central subchannel exhibited a periodic pattern featuring three peaks per pitch. As the axial height increased, the TSFI intensified near the spacer wire. Similarly, edge channels demonstrated periodicity with one peak per pitch and exhibited relatively high TSFI intensities. This pattern was attributable to the uniform rotational direction of the spacer wires on each fuel rod in the traditional model, which facilitated counterflows between the gaps in the outer fuel rods and between the outer and central rods. Consequently, two opposing transverse flows developed within the subchannels. A more pronounced transverse flow with higher velocity occurred behind the spacer wires and intensified closer to them. Here, part of the coolant, driven by the spacer wires, moved along the wrap rotation direction, whereas another portion created a transverse flow in the narrow space, moving opposite to the wrap rotation. The pressure differences and velocity gradients in these regions resulted in vortex formation. This reverse flow phenomenon may disrupt coolant circulation, adversely affecting the heat transfer and pressure drop within the assembly.

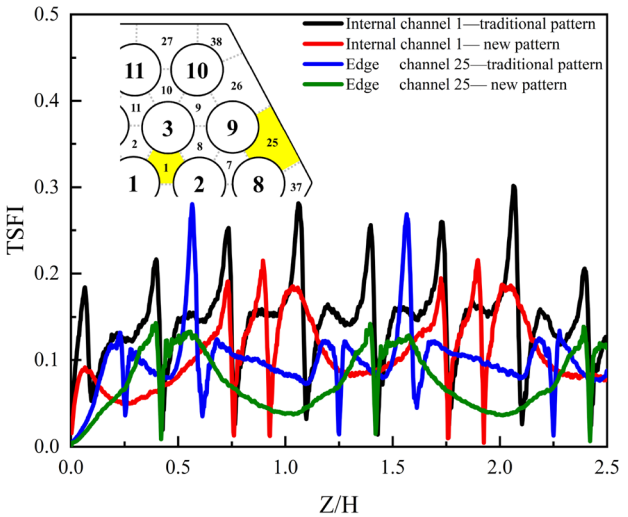

Fig. 10 (Color online) Transverse secondary flow distribution in the axial direction

In the new-pattern fuel assembly, the TSFI distribution within the central subchannel exhibited dynamic changes. The TSFI variation was particularly noticeable near the axial heights of 1 H and 2 H, which were characterized by persistent peaks and troughs. Meanwhile, TSFI in the edge channels varied more subtly with increasing axial height and maintained a lower intensity than that in the edge channels of the traditional model. The innovative design of the fuel assembly in the new model generated distinct coolant flow patterns compared to the original design. The opposite wire-wrap rotation directions on the fuel rods adjacent to the central subchannel prevented the reverse flow of the coolant in the gaps between the rods. On the surfaces of the fuel rods, the coolant flowed consistently along the forward direction. This distinct design feature resulted in the wrapping of adjacent rods that intersected within the same subchannel, leading to the formation of paired vortex structures. Consequently, the central subchannel experienced diverse influences from the wraps rotating in different directions, thereby inducing both clockwise and counterclockwise vortices, which increased the TSFI. In contrast, the edge channels affected by only one spacer wire exhibited a reduced TSFI. The steady coolant flow in the new model enhanced the turbulent mixing across subchannels.

3.3 Temperature distribution characteristics and heat transfer efficiency analysis

Figure 11 presents the temperature contours at axial heights of 90 mm, 180 mm, 270 mm, and 360 mm within the fuel assemblies of both traditional and new model designs. The fuel assembly of the traditional model exhibited an uneven temperature distribution across various cross-sections, characterized by distinct hot and cold areas. Here, the centrally located stainless-steel rod, devoid of a heat source, contributed to the lower temperatures in the central subchannel. Conversely, the fuel assembly of the new model showed a more symmetrical temperature profile in different cross-sections, with notably uniform temperatures in the central subchannel. This uniformity was attributed to the enhanced convective heat transfer facilitated by the strong crossflow and vortex formation in the gaps between the fuel rods. Figure 10 indicates a substantial transverse secondary

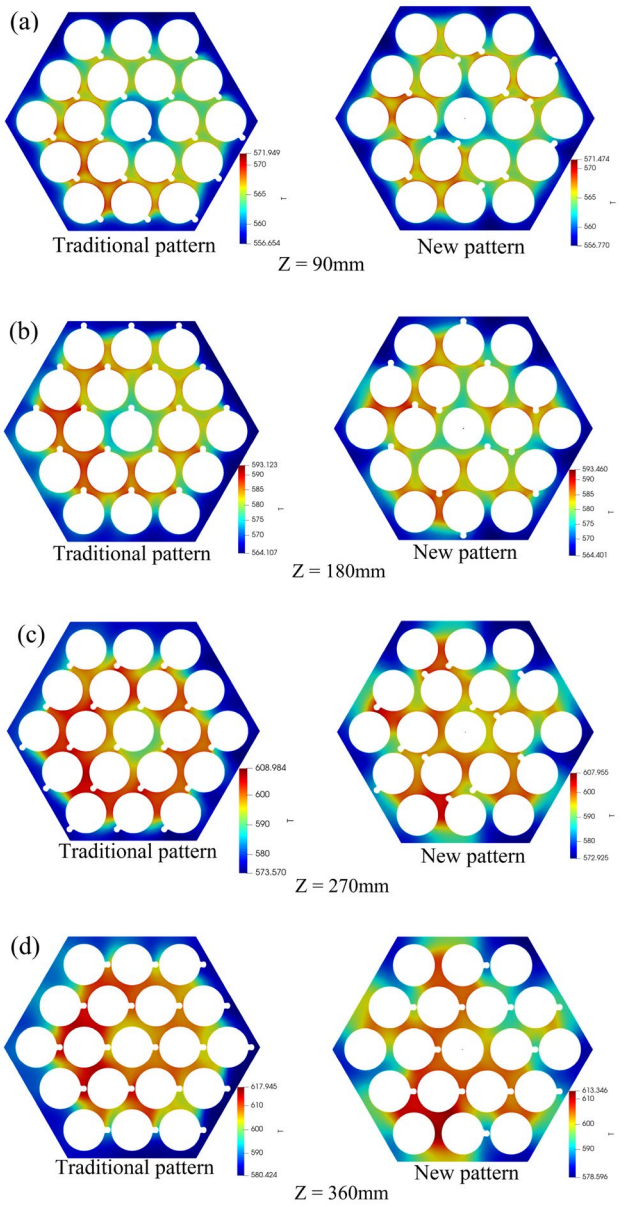

Fig. 11 (Color online) Comparison of the radial temperature distribution at different axial heights. **a** $Z = 90$ mm; **b** $Z = 180$ mm; **c** $Z = 270$ mm; **d** $Z = 360$ mm

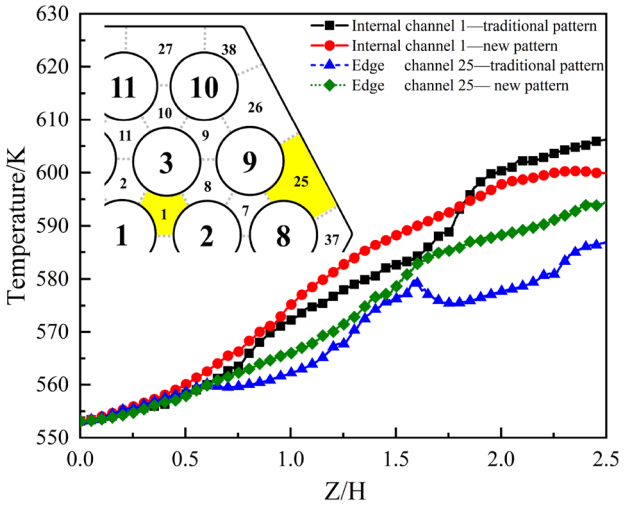

Fig. 12 (Color online) Comparison of the coolant temperature along the axial direction in different subchannels

flow within the internal channels of the fuel assembly in the proposed model. The enhanced lateral secondary flow facilitated turbulent mixing of the coolant in the internal channels. By redesigning the spacer wire distribution and rotation pattern, the coolant flow within subchannels was more evenly distributed, leading to a more balanced temperature profile in the new model. The highest temperature in the cross section typically occurred at points where the fuel rods contacted the spacer wires. The stagnant flow near these spacer wires, coupled with the reduced flow velocity of the liquid lead–bismuth coolant, resulted in localized heat transfer deterioration and an elevated temperature. Moreover, redesigning the wire-wrap distribution and rotation patterns also diminished the local hot spots and overheating within the assembly.

Figure 12 presents a comparison of the axial temperature distribution along internal channel 1 and edge channel 25 in the traditional and new model fuel assemblies. In the traditional model, an increase in the axial height correlated with amplified temperature fluctuations in the coolant. Specifically, the temperature in the internal channel exhibited a more rapid increase, reaching higher values, whereas that in the edge channel increased more gradually with less variation. As per Fig. 9, the heightened flow velocity of the coolant in the edge channels near the assembly box, coupled with incomplete heating, resulted in lower temperatures in these areas. In contrast, the fuel assembly of the proposed model exhibited a more consistent and less fluctuating increase in the coolant temperature with axial height. This steadiness was owing to the absence of spacer wires on the central stainless-steel rod and a redesigned wrap rotation pattern on the surrounding fuel rods, which resulted in a redistributed coolant flow in the central subchannel. The improved mixing of the coolant in the central subchannel enhanced the flow and heat transfer between the coolant and fuel rods, facilitating greater heat absorption and dissipation. Consequently, the heat transfer efficiency of the fuel assembly designed using the proposed model notably increased near the midpoint of the assembly. Compared to the traditional model, the central subchannel in the new model offered a larger flow area and reduced flow resistance, promoting a more uniform temperature increase. Decreasing the coolant flow resistance enhanced the

convective heat exchange between the coolant and the fuel rods. The fuel rods at the six corners of the new pattern fuel assembly had no spacer wires. The edge channel was primarily affected by the rotation of a single spacer wire. The mixing effect of the spacer wire ensured a gentle and stable increase in the coolant temperature in the edge channel.

The heat transfer from the fuel rod to the coolant occurs via convective processes. The convective heat transfer coefficient (h) is quantified as the ratio of the wall heat flux density (q_w) to the temperature differential between the solid surface and fluid. The formula for this calculation is as follows:

$$h = \frac{q_w}{T_s - T_f}. \tag{18}$$

Figure 13 illustrates the axial distribution of the convective heat transfer coefficient, h, in internal channel 1 and edge channel 25. As observed in Fig. 13a, the coefficient in internal channel 1 of the traditional model fuel assembly exhibited pronounced oscillations along the axial direction. In comparison, the proposed model's fuel assembly exhibited more subdued fluctuations. The average convective heat transfer coefficient in the internal channel was higher in the new model than in the traditional model, including the peak values. This increase was attributed to the complex flow field within the internal channel resulting from intense coolant mixing, which subsequently enhanced the heat transfer between the coolant and fuel rods. The innovative design of the new model, which altered the spacer wire rotation pattern and arrangement, contributed to this improved mixing. Thus, the convective heat transfer coefficient increased. This innovative design approach enhanced the heat transfer and thermal exchange efficiency, thereby minimizing the temperature disparity between the fuel rod surfaces and coolant. It also mitigated the risk of localized overheating, combats thermal fatigue, and diminished thermal stress, potentially prolonging the lifespan of the fuel rods in the central subchannel. Figure 13b reveals that in the edge channel 25, the convective heat transfer coefficient exhibits greater oscillations, with the amplitude increasing alongside the axial height. However, the new model fuel assembly demonstrated less variability in the edge channel than the traditional model. The removal of the wire wraps from the fuel rods at the six corners of the new model fuel assembly diminished the lateral flow effect of the coolant in the edge channels. This decreased lateral flow may affect the heat exchange efficiency of the coolant within the assembly. The convective heat transfer performance of the new model in the edge channel surpassed that of the traditional model, particularly near the assembly outlet, where its efficiency significantly exceeded that of the traditional model.

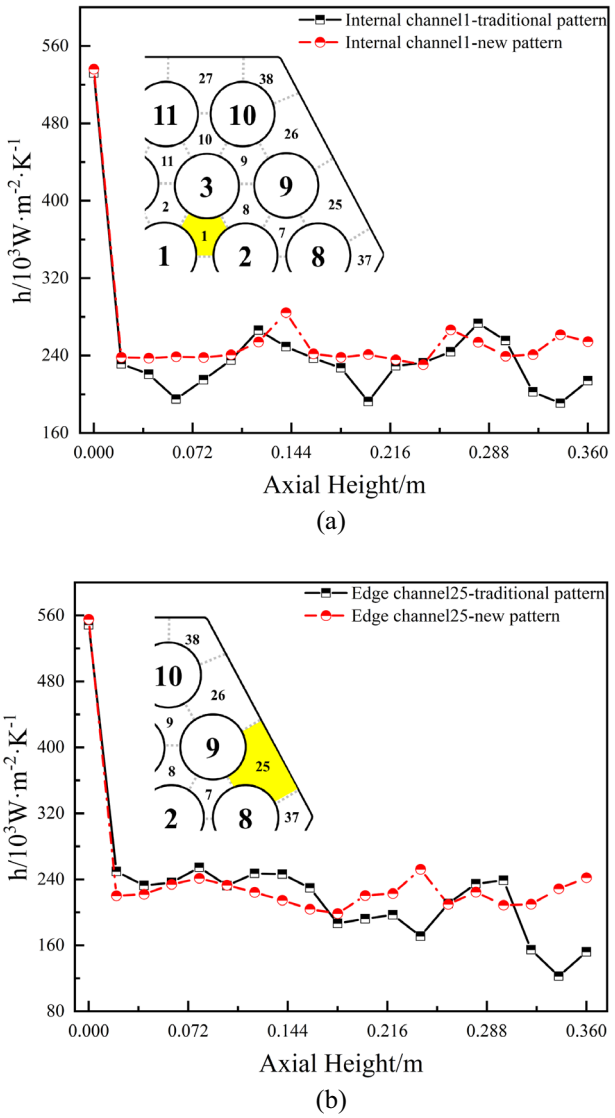

Fig. 13 (Color online) Comparison of convective heat transfer coefficients along the axial direction. **a** Comparison of convective heat transfer coefficients along the axial direction_internal channel 1; **b** comparison of convective heat transfer coefficients along the axial direction_edge channel 25

3.4 Comprehensive thermal-hydraulic performance comparison

By analyzing the flow and heat transfer dynamics of various fuel components, a correlation between coolant flow and heat transfer within these components was identified. The pressure drop factor (f) serves as an indicator of the flow characteristics within the components and is determined by the extent of the pressure drop. A higher value of f signifies increased pressure loss as the coolant traverses through the components. Conversely, the Nusselt number (Nu) indicates the effectiveness of heat transfer within the

components. An elevated Nu value indicates an enhanced heat transfer efficiency of the coolant, which is marked by significant convective heat transfer between the coolant and fuel rods. To holistically evaluate the flow and heat transfer phenomena in fuel components with different designs, an integrated thermal-hydraulic factor (ITHF) was established for comprehensive assessment. The formula for ITHF is

$$\mathrm{ITHF} = \frac{\left(f/f_0\right)^{1/2}}{Nu/Nu_0}, \tag{19}$$

where f_0 and Nu_0 denote the pressure drop factor and global Nusselt number, respectively, for the bare rod component under identical computational conditions. The results of the ITHF calculations for fuel components of various designs are summarized in Table 5.

An analysis of Table 5 reveals that the pressure drop factor for the wire-wrapped fuel assembly exceeded that of the rod assembly, indicating that wire wrapping escalates the pressure loss of the coolant flowing through the assembly. Notably, the friction factor for the new-pattern fuel assembly was lower than that of the traditional pattern, suggesting that the new design mitigated the adverse effects of the pressure drop caused by the spacer wires. The quantity of the wire wrap influenced the pressure drop across the rod bundle section. A decrease in the number of wire wraps resulted in a reduced pressure drop. Furthermore, the innovative design of the new model increased the cross-sectional area of the axial coolant flow, further contributing to the pressure drop reduction. In addition, the new-pattern fuel assembly registered the highest Nusselt number overall, signifying the enhanced heat transfer efficiency of the coolant. This innovative wire-wrap arrangement induced a more robust lateral secondary flow in the internal channels, facilitating turbulent coolant mixing. This improvement enhanced both the flow and heat transfer between the coolant and fuel rods. Considering the combined flow and heat transfer characteristics within the assembly, the new pattern design emerged as the most effective in terms of comprehensive heat transfer performance.

Table 5 Integrated thermal-hydraulic factors for different design fuel assemblies

	Bare rod assembly	Traditional-pattern assembly	New-pattern assembly
f	0.02256	0.04895	0.03619
Nu_{avg}	9.16195	9.24318	15.34233
ITHF	1	1.45996	0.75634

4 Conclusion

The flow and heat transfer characteristics of the coolant within lead-cooled fast reactor fuel assemblies critically influence the safety and efficiency of the reactor systems. In this study, heat transfer calculations were conducted in a liquid lead–bismuth single-phase flow using the open-source CFD platform OpenFOAM. The computational method was validated using experimental data and SACOS-PB subchannel code. OpenFOAM was employed to examine the thermal-hydraulic characteristics of the fuel assembly under the newly designed pattern. This involved the detailed modeling of the fuel assembly's rod bundle segment, incorporation of polyhedral mesh division, use of the k-ω SST turbulence model, and the selection of appropriate boundary conditions. The study culminated in an analysis of parameter distributions such as pressure drop, transverse secondary flow, temperature, convective heat transfer coefficient, and an integrated thermal-hydraulic factor within the rod bundle segment of the new pattern fuel assembly. The conclusions are as follows:

1. The number of spacer wires significantly affected the pressure drop along the rod bundle segment in the fuel assemblies. Compared to the traditional design, the new-pattern fuel assembly exhibited a maximum pressure drop reduction of 31.18% and a decrease of 28.77% at the outlet of the assembly. This innovative design is beneficial for minimizing pump head requirements and sensor range.
2. The new pattern design markedly improved the coolant mixing within the subchannels. The direction wherein the spacer wires rotated affected the coolant mixing between subchannels. In the new pattern, the central subchannel experienced an increased transverse secondary flow intensity, whereas the edge subchannel experienced a decrease relative to the traditional design.
3. The new pattern also achieved a more uniform coolant temperature distribution within the subchannels, as evidenced by a reduced temperature gradient at the assembly outlet. This uniformity was instrumental in diminishing the temperature-gradient-induced fluctuations and uneven temperature distribution, thereby reducing the thermal fatigue and creep in the internal components near the coolant outlet.
4. A comparative analysis of the ITHF revealed that the friction factor for the new-pattern fuel assembly was lower than that of the traditional design, mitigating the adverse effects of pressure drop owing to spacer wires. In addition, the higher overall Nusselt number in the new pattern indicated the superior heat-transfer capabilities of the coolant. Considering both the flow and heat

transfer characteristics, the new-pattern fuel assembly demonstrated superior overall heat transfer performance.

Author Contributions All authors contributed to the study conception and design. Material preparation, data collection and analysis were performed by Y-XL, R-SY, X-KS. The first draft of the manuscript was written by Y-XL and all authors commented on previous versions of the manuscript. All authors read and approved the final manuscript.

Data availibility The data that support the findings of this study are openly available in Science Data Bank at https://cstr.cn/31253.11.sciencedb.j00186.00244 and https://www.doi.org/10.57760/sciencedb.j00186.00244.

Declarations

Conflict of interest The authors declare that they have no conflict of interest.

References

1. J.A. Lake, The fourth generation of nuclear power. J. Prog. Nucl. Energy **40**(3–4), 301–307 (2002). https://doi.org/10.1016/S0149-1970(02)00023-9
2. J. Wang, W.X. Tian, Y.H. Tian et al., Thermal-hydraulic primary numerical analysis for Pb-Bi fast reactor sub-channel. J. At. Energy Sci. Technol. **47**(01), 38–42 (2013) **(in Chinese)**
3. A. Alemberti, V. Smirnov, C.F. Smith et al., Overview of lead-cooled fast reactor activities. J. Prog. Nucl. Energy **77**, 300–307 (2014). https://doi.org/10.1016/j.pnucene.2013.11.011
4. M. Margulis, P. Blaise, E. Gilad, Modeling representative Gen-IV molten fuel reactivity effects in the ZEPHYR ZPR-LFR analysis. Int. J. Energy Res. **43**(02), 829–843 (2019). https://doi.org/10.1002/er.4313
5. Z.X. Gu, H.X. Yu, D.S. Huang et al., Code development and verification of LBE-water interaction under steam generator tube rupture accident for LBE-Cooled Reactor. J. At. Energy Sci. Technol. **57**(07), 1406–1415 (2023) **(in Chinese)**
6. Z.X. Gu, H.X. Yu, D.S. Huang et al., Development and verification of 3D code for steam generator tube rupture accident of LBE-cooled Reactor. J. Nucl. Power Eng. **44**(04), 226–233 (2023) **(in Chinese)**
7. Y.X. Li, L. Meng, S. Li et al., CFD analysis of a CiADS fuel assembly during the steam generator tube rupture accident based on the LBEsteamEulerFoam. Nucl. Sci. Tech. **34**(10), 138–149 (2023). https://doi.org/10.1007/s41365-023-01312-1
8. Z.Y. Gong, Z.X. Gu, Q.W. Pan et al., Development and verification of code for simulation of vapor-liquid two phase 2D pressure wave propagation. Nucl. Tech. **46**(06), 136–146 (2023) **(in Chinese)**
9. H.R. Qiu, M.J. Wang, J. Zhang et al., Multi-scale coupling analysis of the flow blockage accident in the typical LFR. Int. J. Therm. Sci. **195**, 108615 (2024). https://doi.org/10.1016/j.ijthermalsci.2023.108615
10. L. Zhang, Y.W. Yang, Y.C. Cao, Preliminary physics study of the Lead-Bismuth-Eutectic spallation target for China initiative accelerator driven subcritical system. Nucl. Sci. Tech. **27**, 120 (2016). https://doi.org/10.1007/s41365-016-0114-6
11. Z.Q. Liu, Z.L. Zhao, Y.W. Yang et al., Shielding calculation of LBE target flow pipeline in ADS. Nucl. Tech. **41**(3), 030604 (2018). https://doi.org/10.11889/j.0253-3219.2018.hjs.41.030604 **(in Chinese)**
12. J. Wen, T.J. Peng, X.K. Fan et al., Analysis and optimization of flow distribution for the reactor core of China initiative accelerator driven system. Nucl. Tech. **43**, 070601 (2020). https://doi.org/10.11889/j.0253-3219.2020.hjs.43.070601 **(in Chinese)**
13. T.Y. Hui, R. Luo, W.J. Zeng et al., ADS subcritical reactor core power control based on external neutron source intensity. Nucl. Tech. **42**, 080602 (2019). https://doi.org/10.11889/j.0253-3219.2019.hjs.42.080602 **(in Chinese)**
14. X.N. Du, Y.P. Wang, Y.Q. Zheng et al., The steady-state neutronic analysis and transient simulation of ADANES reactor design based on deterministic method. Nucl. Tech. **45**, 100601 (2022). https://doi.org/10.11889/j.0253-3219.2022.hjs.45.100601 **(in Chinese)**
15. T.L. Cong, J.J. Wang, Y. Xiao et al., Analysis of transverse flow characteristics in LBE-cooled wire-wrapped fuel assembly. J. At. Energy Sci. Technol. **56**(12), 2725–2734 (2022) **(in Chinese)**
16. K. Arwikar, H. Fenech, Heat transfer, momentum losses and flow mixing in a 61-tube bundle with wire-wrap. J. Nucl. Eng. Des. **55**(3), 403–417 (1979). https://doi.org/10.1016/0029-5493(79)90119-5
17. M. Nishimura, H. Sato, H. Kamide et al., Investigation on velocity distribution around the wrapping wire in an inner subchannel of fuel pin bundle, in *Paper Presented at 20th International Conference on Nuclear Engineering and the ASME 2012 Power Conference* (California, 2012). https://api.semanticscholar.org/CorpusID:110375295
18. H. Kim, H. Bae, Y.J. Ko et al., Investigations of single-phase flow mixing characteristics in a wire-wrapped 37-pin bundle for a sodium-cooled fast reactor. J. Ann. Nucl. Energy **87**, 541–546 (2016). https://doi.org/10.1016/j.anucene.2015.09.022
19. J. Pacio, M. Daubner, F. Fellmoser et al., Experimental study of heavy-liquid metal (LBE) flow and heat transfer along a hexagonal 19-rod bundle with wire spacers. J. Nucl. Eng. Des. **301**, 111–127 (2016). https://doi.org/10.1016/j.nucengdes.2016.03.003
20. H. Wang, S.Q. Wang, D.G. Liu, PIV measurements of the cross flow induced by a wrapped wire spacer. J. Ann. Nucl. Energy **146**, 107634 (2020). https://doi.org/10.1016/j.anucene.2020.107634
21. S. Yang, Y.P. Zhang, Study on two-phase flow in fluid channel of Lead-Based Fast Reactor Based on OpenFOAM. J. At. Energy Sci. Technol. **54**(09), 1582–1588 (2020) **(in Chinese)**
22. Z.W. Su, T. Zhou, M.Y. Liu et al., Thermophysical properties of liquid lead-bismuth eutectic. Nucl. Tech. **36**(9), 090205 (2013). https://doi.org/10.11889/j.0253-3219.2013.hjs.36.090205 **(in Chinese)**
23. X.M. Wu, Y. Zhang, M.S. He et al., Study on sloshing response characteristics of liquid heavy metal coolant. Nucl. Tech. **42**(04), 040603 (2019). https://doi.org/10.11889/j.0253-3219.2019.hjs.42.040603 **(in Chinese)**
24. Z.X. Gu, Q.X. Zhang, Y. Gu et al., Verification of a self-developed CFD-based multi-physics coupled code MPC-LBE for LBE-cooled reactor. Nucl. Sci. Tech. **32**(5), 52 (2021). https://doi.org/10.1007/s41365-021-00887-x
25. S.Y. Liu, D.L. Yu, H.P. Mei et al., Turbulent-Prandtl-number models for liquid lead-bismuth in triangular rod bundles. Nucl. Tech. **45**(03), 030604 (2022). https://doi.org/10.11889/j.0253-3219.2022.hjs.45.030604
26. V. Roozbeh, S. Kamran, An improved porous media model for nuclear reactor analysis. Nucl. Sci. Tech. **27**, 24 (2016). https://doi.org/10.1007/s41365-016-0016-7
27. A. Ahmad, K.Y. Kim, Three-dimensional analysis of flow and heat transfer in a wire-wrapped fuel assembly, in *Paper Presented at Proceedings of the American Nuclear Society—International Congress on Advances in Nuclear Power Plants 2005* (Korea, 2005)
28. R. Gajapathy, K. Velusamy, P. Selvaraj et al., CFD investigation of helical wire-wrapped 7-pin fuel bundle and the challenges in

modeling full scale 217 pin bundle. J. Nucl. Eng. Des. **237**(24), 2332–2342 (2007). https://doi.org/10.1016/j.nucengdes.2007.05.003
29. K.D. Hamman, R.A. Berry, A CFD simulation process for fast reactor fuel assemblies. J. Nucl. Eng. Des. **240**(9), 2304–2312 (2010). https://doi.org/10.1016/j.nucengdes.2009.11.007
30. J. Fricano, E. Baglietto, A quantitative CFD benchmark for Sodium Fast Reactor fuel assembly modeling. J. Ann. Nucl. Energy **64**, 32–42 (2014). https://doi.org/10.1016/j.anucene.2013.09.019
31. J.H. Jeong, J. Yoo, K.L. Lee et al., Three-dimensional flow phenomena in a wire-wrapped 37-pin fuel bundle for SFR. Nucl. Eng. Technol **47**(5), 523–533 (2015). https://doi.org/10.1016/j.net.2015.06.001
32. D. Dovizio, B. Mikuz, A. Shams et al., Validating RANS to predict the flow behavior in wire-wrapped fuel assemblies. J. Nucl. Eng. Des. **356**, 110376 (2020). https://doi.org/10.1016/j.nucengdes.2019.110376
33. S.P. He, M.J. Wang, J. Zhang et al., Numerical simulation of three-dimensional flow and heat transfer characteristics of liquid lead-bismuth. Nucl. Eng. Technol. **53**(6), 1834–1845 (2021). https://doi.org/10.1016/j.net.2020.12.025
34. H.R. Qiu, J. Li, Z.Y. Dong et al., Numerical study on inter-wrapper flow and heat transfer characteristics in liquid metal-cooled fast reactors. Prog. Nucl. Energy **155**, 104534 (2023). https://doi.org/10.1016/j.pnucene.2022.104534
35. O. Bovati, M. Yildiz, Y. Hassan et al., RANS simulations for transition and turbulent flow regimes in wire-wrapped rod bundles. Int. J. Heat Fluid Flow **90**, 108838 (2021). https://doi.org/10.1016/j.ijheatfluidflow.2021.108838
36. O. Bovati, Y. Alper, Y. Hassan et al., Pressure drop and flow characteristics in partially blocked wire wrapped rod bundles. J. Ann. Nucl. Energy **165**, 108671 (2022). https://doi.org/10.1016/j.anucene.2021.108671
37. O. Bovati, Y. Hassan, Numerical study of the impact of blockages on the thermal-hydraulic performance of 19 and 61-pin Wire-Wrapped bundles with conjugate heat transfer using RANS. J. Ann. Nucl. Energy **194**, 110122 (2023). https://doi.org/10.1016/j.anucene.2023.110122
38. Y.D. Li, M. Huang, X.P. Ouyang et al., Numerical study on a 7-pin bundle fuel assembly with different wire arrangements. Prog. Nucl. Energy **168**, 105016 (2024). https://doi.org/10.1016/j.pnucene.2023.105016
39. N. Li, G.Q. Ding, Y. Xiao et al., Numerical study of the influence of rolling motion on the spacer effect of low flow convective heat transfer. J. Nucl. Power Eng. **44**(6), 54–62 (2023) **(in Chinese)**
40. Y.X. Li, L. Meng, Z.N. Huang et al., Study on the effects from spacer wires on coolant flow within a CiADS fuel assembly. J. Ann. Nucl. Energy **183**, 109647 (2023). https://doi.org/10.1016/j.anucene.2022.109647
41. X.K. Su, X.W. Li, X.Y. Wang et al., Development and assessment of an isotropic four-equation model for heat transfer of low Prandtl number fluids. Front. Energy Res. **10**, 816560 (2022). https://doi.org/10.3389/fenrg.2022.816560
42. X.K. Su, L. Gu, T.J. Peng et al., Research on a four-equation model based on OpenFOAM. J. Nucl. Power Eng. **42**(S1), 26–32 (2021) **(in Chinese)**
43. X.K. Su, Numerical study on turbulent heat transfer of liquid lead bismuth based on an isotropic four-equation model. Thesis M. A. University of Chinese Academy of Sciences (Institute of Modern Physics, Chinese Academy of Sciences) (2022) **(in Chinese)**
44. X. Cheng, N.I. Tak, Investigation on turbulent heat transfer to lead-bismuth eutectic flows in circular tubes for nuclear applications. J. Nucl. Eng. Des. **236**(4), 385–393 (2006). https://doi.org/10.1016/j.nucengdes.2005.09.006
45. T.J. Peng, L. Gu, D.W. Wang et al., Conceptual design of subcritical reactor for China Initiative Accelerator Driven System. J. At. Energy Sci. Technol. **51**(12), 2235–2241 (2017) **(in Chinese)**
46. J.T. Liu, Research on subchannel analysis method of lead-based fast reactor fuel assembly with wire spacers for CiADS. Thesis M. A. University of Chinese Academy of Sciences (Institute of Modern Physics, Chinese Academy of Sciences) (2021) **(in Chinese)**
47. K. Natesan, T. Sundararajan, A. Narasimhan et al., Turbulent flow simulation in a wire-wrap rod bundle of an LMFBR. J. Nucl. Eng. Des. **240**(5), 1063–1072 (2010). https://doi.org/10.1016/j.nucengdes.2009.12.025
48. Z.F. Ge, T. Zhou, Y.Q. Bai et al., Thermal-hydraulic analysis in wire-wrapped fuel assembly for China Lead-based Research Reactor. J. At. Energy Sci. Technol. **49**(S1), 167–173 (2015) **(in Chinese)**
49. Z.W. Zhou, Numerical study of flow behavior of lead-bismuth in fuel assembly with wire spacer. Thesis M. A. University of Science and Technology of China (2014) **(in Chinese)**
50. OECD, *Handbook on Lead-Bismuth Eutectic Alloy and Lead Properties, Materials Compatibility, Thermal Hydraulics and Technologies* (OECD, France, 2007)
51. F.R. Menter, Two-equation eddy-viscosity turbulence models for engineering applications. AIAA J. **32**(8), 1598–1605 (1994). https://doi.org/10.2514/3.12149
52. E. Merzari, P. Fischer, H. Yuan et al., Benchmark exercise for fluid flow simulations in a liquid metal fast reactor fuel assembly. J. Nucl. Eng. Des. **298**, 218–228 (2016). https://doi.org/10.1016/j.nucengdes.2015.11.002
53. J. Deng, Q. Lu, D. Wu et al., Sub-channel code development of lead-bismuth eutectic fast reactor available for multiple fuel assembly structures. J. Ann. Nucl. Energy **149**, 107769 (2020). https://doi.org/10.1016/j.anucene.2020.107769
54. K.F. Lv, Study on the thermal-hydraulic behaviors of a wire-wrapped rod bundle cooled with lead bismuth eutectic. Thesis M. A. University of Science and Technology of China (2016) **(in Chinese)**
55. S.K. Chen, Y.M. Chen, N.E. Todreas, The upgraded Cheng and Todreas correlation for pressure drop in hexagonal wire-wrapped rod bundles. J. Nucl. Eng. Des. **335**, 356–373 (2018). https://doi.org/10.1016/j.nucengdes.2018.05.010
56. K. Rehme, Pressure drop correlations for fuel element spacers. Nucl. Technol. **17**, 15–23 (1973). https://doi.org/10.13182/NT73-A31250
57. E. Novendstern, Turbulent flow pressure drop model for fuel rod assemblies utilizing a helical wire-wrap spacer system. J. Nucl. Eng. Des. **22**(1), 28–42 (1972). https://doi.org/10.1016/0029-5493(72)90058-1
58. W.H. Qu, High-resolution measurement for flow characteristics in rod bundle fuel assembly and sub-channel mixing model development. Thesis M. A. Shanghai Jiao Tong University (2019) **(in Chinese)**